Robotics and Computer Integrated Manufacturing 61 (2020) 101852

Contents lists available at ScienceDirect

Robotics and Computer Integrated Manufacturing

journal homepage: www.elsevier.com/locate/rcim

Modelling the dynamics of industrial robots for milling operations

Hoai Nam Huynh*[a], Hamed Assadi[c], Edouard Rivière-Lorphèvre[b], Olivier Verlinden[a], Keivan Ahmadi[c]

[a] Theoretical Mechanics, Dynamics and Vibrations unit, University of Mons, Place du Parc 20, Mons 7000, Belgium
[b] Machine Design and Production Engineering unit, University of Mons, Place du Parc 20, Mons 7000, Belgium
[c] Faculty of Engineering, University of Victoria, Finnerty Road Engineering Office Wing 3800, Victoria BC V8P 5C2, Canada

ARTICLE INFO

Keywords:
Identification
Milling
Modal analysis
Robot

ABSTRACT

Using industrial robots as machine tools is targeted by many industries for their lower cost and larger workspace. Nevertheless, performance of industrial robots is limited due to their mechanical structure involving rotational joints with a lower stiffness. As a consequence, vibration instabilities, known as chatter, are more likely to appear in industrial robots than in conventional machine tools. Commonly, chatter is avoided by using stability lobe diagrams to determine the stable combinations of axial depth of cut and spindle speed. Although the computation of stability lobes in conventional machine tools is a well-studied subject, developing them in robotic milling is challenging because of the lack of accurate multi-body dynamics models involving joint compliance able of predicting the posture-dependent dynamics of the robot. In this paper, two multi-body dynamics models of articulated industrial robots suitable for machining applications are presented. The link and rotor inertias along with the joint stiffness and damping parameters of the developed models are identified using a combination of multiple-input multiple-output identification approach, computer-aided design model of the robot, and experimental modal analysis. The performance of the developed models in predicting posture-dependent dynamics of a KUKA KR90 R3100 robotic arm is studied experimentally.

1. Introduction

Robotic machining is a new application for robots that are usually involved in handling, pick and place, assembling or welding tasks. Compared to conventional machine tools, milling with robots offers a larger workspace at a lower cost but to the detriment of accuracy. Indeed, most of industrial robots are designed as open serial chains with rotational joints which lower their rigidity. During the milling operation, process forces applied at the tool tip can lead to significant trajectory deviation and excessive vibrations. Targeted fields of application are mainly the aeronautics industry, in which large parts are being machined, as well as the foundry industry for finishing operations on parts with complex shapes. Soft materials such as wood, plastic, foam or aluminium can be machined with an accuracy close to conventional machine tools whereas thin layers of hard material such as steel or inconel can hardly be removed [1].

The low joint stiffness of robots is known as the main drawback since process forces exciting the structure may lead to milling instabilities known as *chatter*. Consequences of self-excited vibrations range from a shorter tool life, poor surface finish to a defective spindle. While significant research has been carried out in conventional machining [2–5] in order to predict stable cutting conditions using stability lobe diagrams, few similar studies have been completed in robotic machining. Due to the lack of joint stiffness, milling with robots leads to other sources of instability. Though regenerative chatter is usually considered as the main source of instability in CNC machines when the tool cuts a surface already machined [6], Pan and Zhang [7] pointed out that mode coupling chatter was the dominant source of instability in robotic machining. Since the robot dynamics is driven by its flexible joints, milling forces tend to excite the lower frequency modes. In order to cope with the lack of joint stiffness, Zargarbashi et al. [8] proposed a kinetostatic index to optimize the robot posture for five-axis machining task. Mousavi et al. [9,10] presented two types of robot modelling by considering either only the joint flexibility or their combination with the link flexibility in order to predict the robot dynamic behaviour in different postures. Identification of link elastic properties was carried out on the basis of CAD models and FEM methods. The second modelling was later used to predict the areas of the workspace in which

* Corresponding author.
E-mail addresses: hoainam.huynh@umons.ac.be (H.N. Huynh), hamedassadi@uvic.ca (H. Assadi), edouard.rivierelorphevre@umons.ac.be (E. Rivière-Lorphèvre), olivier.verlinden@umons.ac.be (O. Verlinden), kvahmadi@uvic.ca (K. Ahmadi).

https://doi.org/10.1016/j.rcim.2019.101852
Received 31 March 2019; Received in revised form 18 June 2019; Accepted 7 August 2019

milling operations would be stable [11]. Mejri et al. [12,13] stated that a significant variability in the modal parameters could be observed depending on the robot configuration and suggested that this effect needed to be taken into account in the stability prediction. Most recent studies [14,15] also recommended to consider the cross coupling terms of the tool tip frequency response function matrix in analysing the stability of milling.

Although a multi-body modelling of the robotic arm would be ideal to predict the varying dynamic behaviour of the robot in its workspace, an accurate joint modelling is still challenging. While some authors [16,17] only consider joint flexibility around the axes of motion, others take into consideration a flexibility perpendicular to the joint axis using the so-called *Virtual Joint Modeling* (VJM) method to model the tilting rigidity of the bearings [18–20]. In more complex models, a non linear stiffness is introduced around the joint axis or additionally hysteresis of the gear-torque is considered [21–23]. However, the joint stiffness and damping identification is still an open issue as no straightforward method exists to map the robot dynamic behaviour in its entire workspace. Local identification methods allow determining each joint stiffness around the axis of motion separately. For instance, Olabi et al. [24] hanged dead weights at various locations of their robot to display the stiffness characteristics of each axis. On the other hand, global methods identify all robot rotational stiffness at once but often require expensive equipment or fastidious set-up. Dumas et al. [25] proposed a method which is robust for joint stiffness identification around the axes of motion but needs the use of a laser tracker [26,27]. The aforementioned methods do not provide any information about the robot modal characteristics which are of the highest importance to predict the milling stability. Therefore, experimental modal analysis techniques are used to measure the natural frequencies, the mode shapes and an estimation of the modal dampings. Past studies mimicked the procedure used in CNC machine by measuring the frequency response functions (FRFs) at the tool tip [12,15]. More recently, the robot dynamics was mapped for a restrained milling area in front of the manipulator [28].

In this paper, a straightforward approach to identify the inertial and elastic parameters of a Multi-Body Dynamics (MBD) model of an industrial robot is presented and experimentally validated. The link and rotor inertias along with the joint stiffness and damping parameters of a robotic arm are determined using a combination of rigid body identification method and experimental modal analysis (EMA). The novel approach is based on the identification of robot inertial parameters using exciting trajectories followed by a model updating in a static posture. Elastic parameters are determined in a posture suitable for milling operations and used to predict the robot dynamic behaviour in robot configurations beyond the milling area.

2. Multi-body dynamics with flexible joints

Using the augmented link representation for n-link serial manipulators, the Craig's convention is adopted [29] to describe the kinematics of the Kuka KR90 R3100 robot by only considering the first three revolute joints (Fig. 1a). Joint i connects links $i-1$ and i, and a local coordinate system (x_i, y_i, z_i) is attached to link i.

The origin O_i of frame (x_i, y_i, z_i) is located at the intersection of joint i axis and the common normal to axes of joints $i-1$ and i. Joint angles q_i are measured around the axes of motion of the manipulator oriented along z_i. Mass m_i of each link i is assumed to be non-zero, and vector $\mathbf{C}_i = [C_{xi} \;\; C_{yi} \;\; C_{zi}]^T$ locates the centre of mass of link i in the corresponding local frame. Tensor $\mathbf{I}_i$ defines the moment of inertia matrix of link i around O_i in frame i:

$$\mathbf{I}_i = \begin{bmatrix} I_{xxi} & I_{xyi} & I_{xzi} \\ I_{yxi} & I_{yyi} & I_{yzi} \\ I_{zxi} & I_{zyi} & I_{zzi} \end{bmatrix}. \tag{1}$$

The inertial parameters of each link consist of ten parameters including m_i, m_iC_{xi}, m_iC_{yi}, m_iC_{zi}, I_{xxi}, I_{yyi}, I_{zzi}, I_{xyi}, I_{xzi}, and I_{yzi}. Considering the typically large gear ratios of industrial manipulators, the inertia of the joint rotors may have a significant effect on robot dynamics. As shown in Fig. 1b, the motor actuating joint i is located on link $i-1$ and its axis is aligned with z_i. The joint rotors are assumed to be cylindrical and therefore their inertia tensor with respect to (x_i, y_i, z_i) is described as a diagonal matrix $I_{mi} = diag(I_{m,xxi}, I_{m,yyi}, I_{m,zzi})$ with $I_{m,xxi} = I_{m,yyi}$.

The Multi-Body Dynamics model of the manipulator with three flexible revolute joints is shown in Fig. 1b. The system consists of seven bodies, including the ground (body 0), three links, and the three associated motors. The stiffness and the damping at the interface between each link are modelled by three torsional springs and viscous dampers around x_i, y_i, and z_i axis. More specifically, flexibility q_i around rotation axis z_i accounts for the elasticity between each rotor and its actuated link while q_{ix} and q_{iy} are transversal elasticities around x_i and y_i axes representing the bearing compliance. Among the twelve degrees of freedom of the model in Fig. 1b only three (q_{m1}, q_{m2}, and q_{m3}) are actuated, which makes the identification of the inertia and elastic parameters of this model challenging. In the next section, the model in Fig. 1b is simplified to a system comprising the three motors and a joint flexibility only around the rotation axis, namely the *SDOF flexible joint model*. The inertia and elastic parameters of the simplified system will be identified using exciting trajectories and experimental modal analysis in Sections 2.2 and 3. The identified parameters will eventually be used to calibrate the model parameters of the generalized model in Fig. 1b, namely the *3DOF flexible joint model*.

2.1. MBD with SDOF joint model

The equation governing the dynamics of the system shown in Fig. 1b when only the joint flexibility around its rotation axis z_i is considered can be obtained using Lagrange's method as follows [30]:

$$\begin{Bmatrix} \tau_{ext} \\ \tau \end{Bmatrix} = \begin{bmatrix} \mathbf{M}(\mathbf{q}) & \mathbf{0} \\ \mathbf{0} & \mathbf{M}_m \end{bmatrix} \begin{Bmatrix} \ddot{\mathbf{q}} \\ \ddot{\mathbf{q}}_m \end{Bmatrix} + \begin{bmatrix} \mathbf{C}(\mathbf{q}, \dot{\mathbf{q}}) + \mathbf{F}_{vq} + \mathbf{D} & -\mathbf{D} \\ -\mathbf{D} & \mathbf{F}_{vq_m} + \mathbf{D} \end{bmatrix} \begin{Bmatrix} \dot{\mathbf{q}} \\ \dot{\mathbf{q}}_m \end{Bmatrix}$$
$$\begin{bmatrix} \mathbf{K} & -\mathbf{K} \\ -\mathbf{K} & \mathbf{K} \end{bmatrix} \begin{Bmatrix} \mathbf{q} \\ \mathbf{q}_m \end{Bmatrix} + \begin{bmatrix} \mathbf{F}_{cq} & \mathbf{0} \\ \mathbf{0} & \mathbf{F}_{cq_m} \end{bmatrix} \begin{Bmatrix} sgn(\dot{\mathbf{q}}) \\ sgn(\dot{\mathbf{q}}_m) \end{Bmatrix} + \begin{bmatrix} \mathbf{G}(\mathbf{q}) \\ \mathbf{0} \end{bmatrix}, \tag{2}$$

where $\mathbf{q} = [q_1 \;\; \cdots \;\; q_n]^T$ is the instantaneous angular position of the links and $\mathbf{q}_m = [q_{m1} \;\; \cdots \;\; q_{mn}]^T$ is the corresponding positions of the rotors after reduction gears. The inertia matrix in Eq. (2) consists of the augmented link inertia matrix, $\mathbf{M}(\mathbf{q})$ and rotor inertia matrix, $\mathbf{M}_m$. Considering the typically high gear ratio of industrial robot joints, the coupling between the rotor and link inertia terms is neglected. The augmented link inertia is a non linear function of the joint configuration $\mathbf{q}$ and contains the link inertia terms as well as $N_iI_{m,xxi}$ and $N_iI_{m,yyi}$ terms in the off-diagonal elements, where N_i is the gear ratio of joint i. The rotor inertia matrix, $\mathbf{M}_m$, is a diagonal matrix of $N_i^2I_{m,zzi}$ terms. The damping matrix, $\mathbf{C}(\mathbf{q}, \dot{\mathbf{q}})$, is a non linear function of joint positions and velocities and represents the centrifugal and Coriolis forces. The gravity vector is denoted by $\mathbf{g}(\mathbf{q})$. The $\mathbf{F}_{vq}$ and $\mathbf{F}_{vq_m}$ terms represent the viscous friction forces applied on the link and the rotor, respectively, and $\mathbf{F}_{cq}$ and $\mathbf{F}_{cq_m}$ are the Coulomb friction terms. The $\mathbf{K}$ and $\mathbf{D}$ matrices are diagonal matrices of the joint stiffness and damping coefficients. The actuation torque applied on the rotors is denoted by $\boldsymbol{\tau}$ and the combined effects of the gravity compensation spring and the milling forces act as an external torque $\boldsymbol{\tau}_{ext}$.

The KUKA KR90 arm includes a gravity compensation system that acts like a spring to reduce the gravity load on the second joint. Following the approach presented by Swevers et al. [31], the torque generated by the gravity compensation arm is approximated using the following Fourier series expansion:

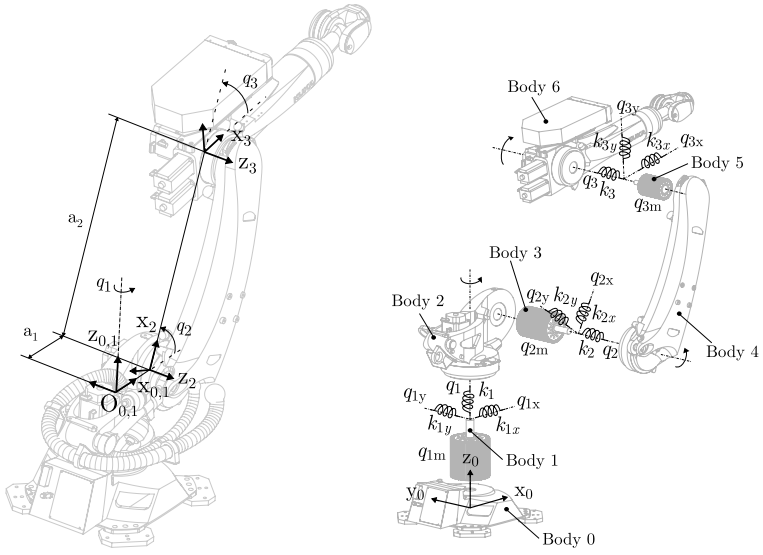

(a) Kinematic model (b) MBD model with flexible joints

Fig. 1. Modelling of the KUKA KR90 R3100 robot.

$$T_g = \sum_{l=1}^{L} B_l \cos(l q_2). \tag{3}$$

In this work, three terms ($L = 3$) in the Fourier series expansion were used to approximate the torque generated by the gravity compensation arm. The resulting torque T_g is substituted in the second element of $\boldsymbol{\tau}_{ext}$ in Eq. (2) to consider the additional external torque provided to the second joint by the gravity compensation arm.

2.2. Identification of rigid body dynamics

In the absence of machining forces, the joint flexibilities can be neglected resulting in the simplification of the equations of motion in Eq. (2) into the following:

$$[\mathbf{M}(\mathbf{q}) + \mathbf{M}_m]\ddot{\mathbf{q}} + \mathbf{C}(\mathbf{q}, \dot{\mathbf{q}})\dot{\mathbf{q}} + \mathbf{g}(\mathbf{q}) + \underbrace{\left(\mathbf{F}_{vq} + \mathbf{F}_{vq_m}\right)\dot{\mathbf{q}}}_{F_v} + \underbrace{\left(\mathbf{F}_{cq} + \mathbf{F}_{cq_m}\right)}_{F_c} sgn(\dot{\mathbf{q}}) = \tau + \tau_{ext}. \tag{4}$$

This equation is linear in terms of the base parameters of the manipulator [32], and can therefore be reformulated as the following linear equation:

$$\mathbf{Y}\boldsymbol{\pi} = \tau, \tag{5}$$

where the components of the vector of base parameters, π, and the regression matrix $\mathbf{Y}$ are provided in Appendices A and B, respectively. The base parameters of the manipulator are the minimum number of parameters that are required for describing its dynamics uniquely [33]. For the considered system with three motors and their rigid joint, a total of 18 base parameters are required to describe the relationship between the actuating torque, $\boldsymbol{\tau}$, and the resulting joint positions, $\mathbf{q}$, velocities, $\dot{\mathbf{q}}$ and accelerations, $\ddot{\mathbf{q}}$. As shown in Table A.8, in addition to the base parameters combining the inertial parameters of the links and the rotors, viscous and Coulomb friction coefficients and the Fourier coefficients of the function describing the gravity compensating system (i.e. B_1, B_2, and B_3 in Eq. (3)) can be supplemented to enrich the identification procedure. A Multi-Input Multi-Output (MIMO) Least Squares Estimation (LSE) is used to identify the rigid body (base) parameters gathered in vector π. The input signals to the identification are the displacement, velocity, and acceleration signals of the three joints of the manipulator, $\mathbf{q}$. The output signals are the corresponding joint torque signals, $\boldsymbol{\tau}$. These signals are obtained by moving the end effector on optimized trajectories within the workspace of the robot and recording the joint encoder and motor torque signals at a set of discrete time instants, $t_1, ..., t_M$. The system parameters, π, are then obtained using the LSE on a set of equations obtained by repeating Eq. (5) at every time step:

$$\mathbf{A}\pi = \mathbf{T}, \tag{6}$$

where

$$\mathbf{A} = \begin{bmatrix} \mathbf{Y}(\mathbf{q}_1, \dot{\mathbf{q}}_1, \ddot{\mathbf{q}}_1) \\ \vdots \\ \mathbf{Y}(\mathbf{q}_M, \dot{\mathbf{q}}_M, \ddot{\mathbf{q}}_M) \end{bmatrix}, \quad \mathbf{T} = \begin{bmatrix} \tau_1 \\ \vdots \\ \tau_M \end{bmatrix}, \quad \text{and} \quad \tau_i = \tau(t_i), \quad \mathbf{q}_i = \mathbf{q}(t_i). \tag{7}$$

In order to ensure that the obtained torque and joint displacement data are informative [34], persistently excitation trajectories are designed to minimize the condition number of the observation matrix, $\mathbf{A}$, in Eq. (5). The design of such optimum trajectory in joint space was proposed by Swevers et al. [35], where the joint velocity along the trajectory is made of a finite sum of harmonic sine and cosine functions. Finite Fourier series expansions therefore define the time evolution of the joints of the manipulator and their time derivatives as follows:

$$q_i(t) = \sum_{l=1}^{N_i} \frac{a_l^i}{\omega_f l} \sin(\omega_f l t) - \frac{b_l^i}{\omega_f l} \cos(\omega_f l t) + q_{i\,0}, \tag{8}$$

$$\dot{q}_i(t) = \sum_{l=1}^{N_i} a_l^i \cos(\omega_f l t) + b_l^i \sin(\omega_f l t), \tag{9}$$

$$\ddot{q}_i(t) = \sum_{l=1}^{N_i} - a_l^i \omega_f l \sin(\omega_f l t) + b_l^i \omega_f l \cos(\omega_f l t), \tag{10}$$

where ω_f is the assumed fundamental angular frequency of the Fourier series. The constant coefficients, a_l^i and b_l^i, constitute the optimization design parameters, δ, which are determined by minimizing the condition number of the observation matrix, $\mathbf{A}$. The optimization problem is summarized as follows:

$$\hat{\boldsymbol{\delta}} = \arg\ \min_{\delta}\ \text{cond}(\mathbf{A}(\boldsymbol{\delta}, \omega_f)), \tag{11}$$

subjected to

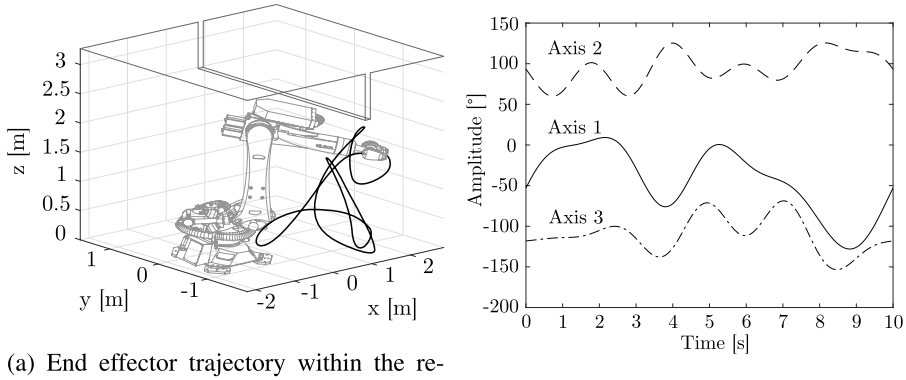

(a) End effector trajectory within the restrained workspace

(b) Corresponding joint trajectories

Fig. 2. Example of excitation trajectory.

$$\begin{cases} \mathbf{q}_{\min} \leqslant \mathbf{q}(pT_s, \boldsymbol{\delta}) \leqslant \mathbf{q}_{\max} \\ \dot{\mathbf{q}}_{\min} \leqslant \dot{\mathbf{q}}(pT_s, \boldsymbol{\delta}) \leqslant \dot{\mathbf{q}}_{\max} \\ \ddot{\mathbf{q}}_{\min} \leqslant \ddot{\mathbf{q}}(pT_s, \boldsymbol{\delta}) \leqslant \ddot{\mathbf{q}}_{\max} \\ \{\mathbf{s}(\mathbf{q}(pT_s, \boldsymbol{\delta}))\} \subset \mathbf{S} \end{cases} \text{for } 0 \leqslant p \leqslant \frac{T_f}{T_s}, \tag{12}$$

with T_s being the sampling period and $T_f = \frac{2\pi}{\omega_f}$. The set of equations shown in Eq. (12) determines the constraints of the optimization problem. These constraints are governed by the displacement, velocity, and acceleration limitations of the joints, and the workspace of the robot. Vectors $\mathbf{q}_{\min}$ and $\mathbf{q}_{\max}$ determine the allowable range of axis displacement, vectors $\dot{\mathbf{q}}_{\min}$ and $\dot{\mathbf{q}}_{\max}$ determine the allowable axis velocity range and vectors $\ddot{\mathbf{q}}_{\min}$ and $\ddot{\mathbf{q}}_{\max}$ determine the allowable axis acceleration range. Also, $\mathbf{S}$ stands for the available workspace while $\mathbf{s}(\mathbf{q})$ is a subset of positions reachable by the end effector of the manipulator according to the optimized trajectories. A sample of optimized end effector trajectory obtained for the KUKA KR90 arm in this work, and the corresponding allowable workspace, is shown in Fig. 2a.

2.3. Experimental results

The identification procedure described in Section 2.2 is applied to determine the parameters of the rigid body model of a KUKA KR90 R3100 HA robotic arm. The architecture of this arm is common to most industrial robots with $a_1 = 0.35$ m and $a_2 = 1.35$ m (Fig. 1a). Only the first three links were considered in this study. Without any tool attached, the third link merges the elbow, the forearm, the wrist and the flange of the robot.

The optimum excitation trajectory was determined by solving the optimization problem defined in Eqs. (11) and (12). Five harmonic terms were considered in the Fourier series expansion of the trajectory of each joint in Eqs. (8)–(10). The fundamental frequency of the excitation trajectory, $\frac{\omega_f}{2\pi}$, was set to 0.1 Hz; a sufficiently low frequency to not excite the joint flexibility. The joint constraints restricting their displacement, velocity, and acceleration are shown in Table 1. Since no joint acceleration limit was provided by the robot manufacturer, high values were set.

Workspace limits are presented in Table 2.

Table 1
Joint angular, velocity and acceleration limits for the KUKA KR90 R3100 HA robot.

Axis	$q_{\min}$ [rad]	$q_{\max}$ [rad]	$\dot{q}_{\min}$ [rad/s]	$\dot{q}_{\max}$ [rad/s]	$\ddot{q}_{\min}$ [rad/s^2]	$\ddot{q}_{\max}$ [rad/s^2]
1	−3.23	3.23	−1.83	1.83	−8	8
2	0.09	2.44	−1.76	1.76	−8	8
3	−2.7	2.1	−1.87	1.87	−8	8

Table 2
Workspace limits.

$x_{\min}$ [m]	$x_{\max}$ [m]	$y_{\min}$ [m]	$y_{\max}$ [m]	$z_{\min}$ [m]	$z_{\max}$ [m]
−1.5	2.6	−1.6	1.4	0.5	2.5

The constrained non linear optimization problem defined in Eq. (11) was solved using the `fmincon` function of Matlab. Starting from various initial values for the optimization parameters, δ, a total of six different excitation trajectories were obtained. The average condition number among the obtained solutions was 28, which was sufficiently low, considering the limited workspace. Fig. 2b depicts the trajectory of each joint for one of the excitation trajectories. The corresponding Tool Centre Point (TCP) trajectory is shown in Fig. 2a. The KUKA KR90 robot was programmed using the `point-to-point spline` command in order to produce smooth motions. Using the `Trace` feature of the KUKA teach pendant, motor torques and encoder positions were recorded using a sampling rate of 250 Hz on a Personal Computer, and the joint velocity and acceleration signals were obtained by numerical differentiation of the encoder data using the FFT filtering method [36]. Prior the numerical differentiation, a low-pass filter was applied to prevent noise magnification with a tapering from unity to zero from 3 to 4 Hz. Application example of the low-pass filter for one of the excitation trajectories is shown in Fig. 3: raw torque and position measurements are compared to their filtered version and numerical differentiation leads to the corresponding acceleration signals. Applying the low-pass filter did not change the position signals which might be due to the internal filtering of KUKA software. The 18 base parameters along with the friction and gravity compensation coefficients were estimated by providing the joint and torque data obtained from four of the six generated trajectories to the LSE problem defined in Eq. (6). The measured and estimated torque signals corresponding to the four trajectories are shown in Fig. 4, as well as their error in Nm. The close agreement of the estimated and measured torque signals confirms the accuracy of the MBD model with rigid joints described with the equations of motion in Eq. (4).

The 27 identified parameters, π, along with the joint position measured during the last two trajectories are eventually used in Eq. (6) to predict the joint torque signals. The predicted and measured torque signals are shown in Fig. 5. As shown in this figure, the identified model accurately estimates the joint torques for arbitrary trajectories.

3. Experimental modal analysis

Modal properties of the KUKA KR90 arm were identified by conducting a set of Experimental Modal Analysis (EMA) tests. Instrumented hammer (Kistler 9722A500) with a rubber tip was used as the

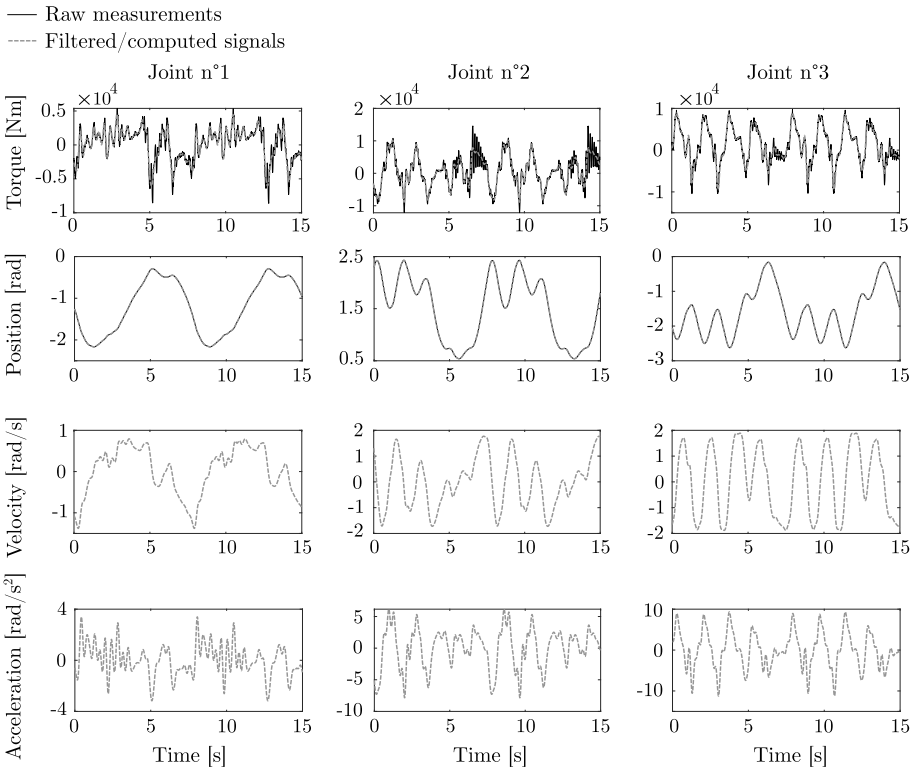

Fig. 3. Raw measurements and filtered/computed signals.

excitation method, and the responses were measured simultaneously using three accelerometers installed on the flange in normal (X), and lateral (Y and Z) directions (Fig. 6). Because of the high rigidity of the system in the direction normal to the flange, a high-sensitivity accelerometer (Kistler 8776A50M1) was used to measure the response in X direction, and two identical miniature accelerometers (PCB 352C23) were used to measure the responses in Y and Z directions. The measured force and acceleration signals were digitized and transferred to a PC using a NI9234 data acquisition card. The Frequency Response Functions (FRFs) were computed using Cutpro software [37]. Implementing the roving hammer technique, impulses were applied at 23 points distributed on the three links of the robot, including the three X, Y, and Z directions on the flange, points x_{21}, y_{21} and z_{21}. The excitation points are shown in Fig. 6. In total, 23×3 FRFs with 0.5 Hz frequency resolution were obtained. The actuator brakes were released when performing the hammer tests to account for the controller stiffness, however repeating the tests with brakes engaged did not make any tangible differences in the measured FRFs, showing that the stiffness of the controller is high enough to be neglected in this analysis.

In order to study the posture-dependent dynamics of the robot structure, EMA was conducted in three different postures shown in Fig. 6. In the rest of this article, *Posture 1* will be referred to as the rigid posture, *Posture 2* as the upright posture, and *Posture 3* as the milling posture.

Modal parameter identification was carried out using the time domain Least Squares Complex Exponential (LSCE) method implemented in the LMS Test.Lab Rev. 8A software. Modal analysis results show that the posture-dependent modes of the structure are located below 30 Hz, and the modes above 30 Hz are mostly influenced by the wrist structure and therefore are independent of the orientation of the first three joints. Consequently, only the modes below 30 Hz will be discussed in this work. The summation function indicator [38] of all the FRFs measured in each posture is shown in Fig. 7. Also shown in this figure are the stabilization diagrams obtained by the LSCE modal identification in each posture. A streak of "s" characters indicates that the identification algorithm converges to a stable mode at the corresponding frequency.

As shown in Fig. 7, in all of the postures, four modes below 30 Hz are identified. The shape, frequency, and modal damping ratio of each of the four identified modes in each posture are shown in Fig. 8. Also shown in this figure are the auto Modal Assurance Criteria (MAC) tables of the identified mode shapes in each posture.

According to the modal analysis results demonstrated in Fig. 8, the mode shapes in all of the postures are originated from the deflections at the joints and the links are rigid. Mode one (10.0 Hz) in the milling posture is greatly influenced by the stiffness of joint one around its rotation axis (q_1). Mode two (11.0 Hz) in this posture is formed by the deflection of the second joint around its rotation axis (q_2), and mode four (23.7 Hz) mainly includes the deflection of the third joint around its rotation axis (q_3). Mode three (19.2 Hz) in the milling posture includes simultaneous deformations of joint one around its rotation axis (q_1) and around the axis normal to it (q_{x1}). While all of the deformations observed in modes one, two, and four are considered in the MBD model with the SDOF joint model, the deflection around x_1 axis is discarded since mode three cannot be simulated by the SDOF joint model. Because deflections around the axes of rotation of joints two and three (q_2 & q_3) generate similar motions in the Cartesian space, a relatively high correlation is observed between modes two and four in the auto-MAC matrix shown in Fig. 8d for the milling posture; same comment apply to modes one and three. Similar modal behaviours are observed in the upright and rigid postures, except that the modal frequencies and their stiffness vary in those postures. In the upright posture, the mode associated with the deflection of joint one around its rotation axis (q_1) is identified as mode three at 20.4 Hz, while modes associated with the deflections of joints two and three around their respective rotation axis (q_2 & q_3) are identified as modes two and four at 11.8 and 25.4 Hz, respectively. Mode one at 11 Hz in the upright posture includes the deflections of the first joint around the axis normal to its rotation axis (q_{x1}) (similar to mode three in the milling posture) and therefore cannot be simulated using the SDOF joint model. In the rigid posture, the third (17.8 Hz) and fourth (22.1 Hz) modes are mainly associated with the

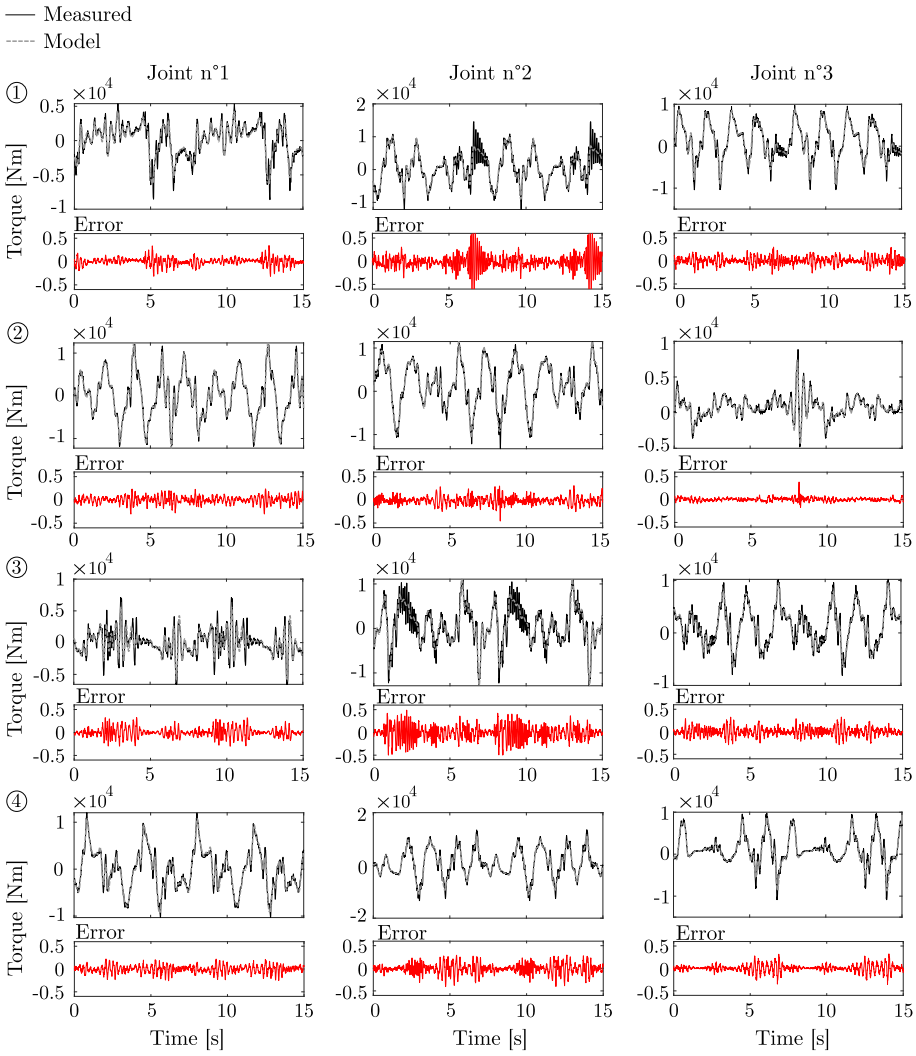

Fig. 4. Fitting of the measured torques over four excitation trajectories.

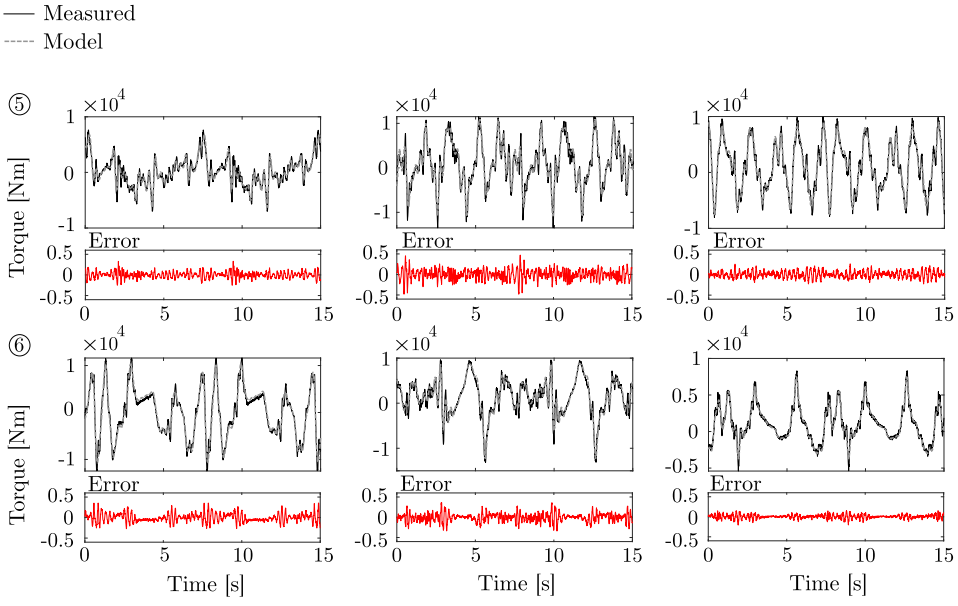

Fig. 5. Torque prediction over two other measured trajectories.

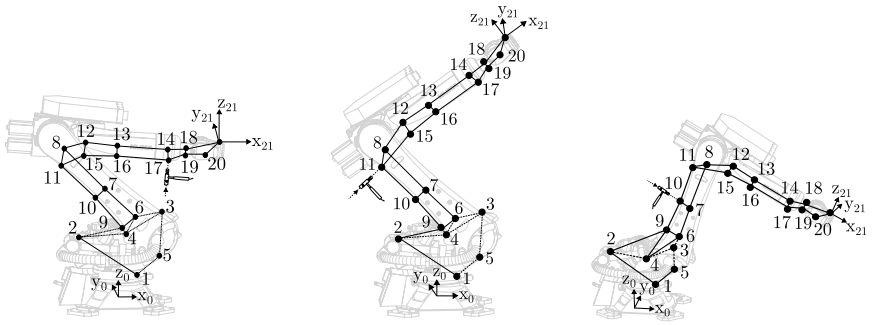

(a) Posture 1: rigid configuration q_1=0°, q_2=135°, q_3=-140°

(b) Posture 2: upright configuration q_1=0°, q_2=135°, q_3=-100°

(c) Posture 3: milling configuration q_1=0°, q_2=70°, q_3=-100°

Fig. 6. Three robot postures studied using EMA.

deflections of the first and third joints around their rotation axis (q_1 & q_3), respectively. According to the stabilization diagram in this posture (Fig. 8a), there are two closely spaced modes at 11 and 11.5 Hz. Note that the frequency resolution of the measured FRFs was 0.5 Hz and therefore the two modes could not be distinguished in the corresponding plot depicting the sum of FRFs (Fig. 7a). According to the identified mode shapes, while mode two is dominated by the deflections of joint two around its rotation axis (q_2), mode one includes deflections of the first joint around the axis normal to its rotation axis (q_{1x}) and therefore it cannot be simulated using the SDOF joint model. Additionally, because the first two modes in the rigid posture are closely spaced, the identified mode shapes are influenced by measurement and identification errors. For instance, deflections of the second and third links are observed in the identified mode shapes, which is highly unlikely to happen at such low frequencies. The auto-MAC matrix of the measured mode shapes includes high correlation between the first and second modes in the rigid postures.

4. Robot structural dynamics

Considering the typically low feedrate during robotic milling operations, the motion of the robot can be regarded as quasi-static where the joint angles, $\mathbf{q}$, only vary incrementally around the operating posture, $\mathbf{q}^0$:

$$\mathbf{q} = \mathbf{q}^0 + \Delta\mathbf{q}. \tag{13}$$

Consequently, the joint velocity and accelerations also vary incrementally around zero:

$$\dot{\mathbf{q}} = \Delta\dot{\mathbf{q}} \quad \text{and} \quad \ddot{\mathbf{q}} = \Delta\ddot{\mathbf{q}}. \tag{14}$$

In addition, by assuming perfect performance of the joint controllers in regularizing the rotor position, the rotor rotation angles are assumed to remain constant at $\mathbf{N_r}\mathbf{q}^0$, where $\mathbf{N_r}$ is the diagonal matrix of joint gear ratios. Considering these assumptions, the equations of motion of the MBD model with the SDOF joint model in Eq. (4) can be simplified into the following equation:

$$\mathbf{M}(\mathbf{q})\ddot{\mathbf{q}} + \mathbf{C}(\mathbf{q}, \dot{\mathbf{q}})\dot{\mathbf{q}} + \mathbf{D}\dot{\mathbf{q}} + \mathbf{K}(\mathbf{q} - \mathbf{q}_m) + \mathbf{g}(\mathbf{q}) = \mathbf{0}. \tag{15}$$

Note that compared to Eq. (2), in Eq. (15), the inertia matrix includes the augmented link inertia term, $\mathbf{M}$, only and the rotor inertia term, $\mathbf{M_m}$, is missing because of the assumption that the rotors are perfectly regularized at zero velocity. Consequently, all the rotor inertia terms must be removed from vector π. Out of the three $I_{m,zzi}$ terms, only $I_{m,zz3}$ can be explicitly identified in Section 2.3 as π_{16}, and $I_{m,zz1}$ and $I_{m,zz2}$ are only implicitly identified as part of π_1 and π_2. Since these values cannot be identified individually, they are assumed to be equal to the identified $I_{m,zz3}$ value. This assumption is reasonable due to the similar size of the motors actuating joints 1, 2, and 3 and their similar gear ratios in the particular case of the KUKA KR90 robot. If it is not the case, authors advise to rely on the gear ratios to scale $I_{m,zz3}$ for the first two rotors. Moreover, since friction and gravity compensation coefficients are mainly related to the rotors, their contributions are also removed from vector π. Therefore, in Eq. (15), damping matrix $\mathbf{D}$ will account for the joint and link damping. Hence, these considerations allow rewriting Eq. (15) in terms of the regression matrix $\tilde{\mathbf{Y}}$ and the base parameter vector $\tilde{\pi}$ without the effects related to the rotors as follows:

$$\tilde{\mathbf{Y}}\tilde{\pi} + \mathbf{D}\dot{\mathbf{q}} + \mathbf{K}(\mathbf{q} - \mathbf{q}_m) = \mathbf{0}. \tag{16}$$

Considering the assumed small deflection of the joints, the non linear equations of motion in Eq. (16) can be linearized around the operational joint configuration, $\mathbf{q}^0$, resulting in the following linear equation describing the oscillations of the system in joint space:

$$\mathbf{M}^0\Delta\ddot{\mathbf{q}} + \mathbf{C}^0\Delta\dot{\mathbf{q}} + \mathbf{K}^0\Delta\mathbf{q} = \mathbf{0}, \tag{17}$$

where the linearized mass ($\mathbf{M}^0$), damping ($\mathbf{C}^0$: combining the effects of the Christoffel $\mathbf{C}$ and damping $\mathbf{D}$ matrices), and stiffness ($\mathbf{K}^0$: combining the effects of the gravity $\mathbf{g}(\mathbf{q})$ and stiffness $\mathbf{K}$ matrices) matrices are obtained as follows:

$$\mathbf{M}^0 = \left.\frac{\partial\tilde{\mathbf{Y}}\tilde{\pi}}{\partial\ddot{\mathbf{q}}}\right|_0; \quad \mathbf{C}^0 = \left.\frac{\partial\tilde{\mathbf{Y}}\tilde{\pi}}{\partial\dot{\mathbf{q}}}\right|_0 + \mathbf{D}; \quad \mathbf{K}^0 = \left.\frac{\partial\tilde{\mathbf{Y}}\tilde{\pi}}{\partial\mathbf{q}}\right|_{\mathbf{q}^0} + \mathbf{K}. \tag{18}$$

All of the parameters of the mass, stiffness, and damping matrices are obtained from the rigid body identifications, except the joint stiffness and damping parameters, $\mathbf{K}$ and $\mathbf{D}$. These parameters will be identified on the basis of the modal analysis results presented in Section 3.

4.1. Identification of joint elastic parameters

By introducing the state vector $\mathbf{q}_s = [\Delta\mathbf{q}^T \quad \Delta\dot{\mathbf{q}}^T]^T$, Eq. (17) can be expressed in its first order form as

$$\hat{\mathbf{A}}\dot{\mathbf{q}}_s + \hat{\mathbf{B}}\mathbf{q}_s = \mathbf{0}, \tag{19}$$

where $\hat{\mathbf{A}}$ and $\hat{\mathbf{B}}$ are the system matrices:

$$\hat{\mathbf{A}} = \begin{bmatrix} \mathbf{C}^0 & \mathbf{M}^0 \\ \mathbf{M}^0 & \mathbf{0} \end{bmatrix}, \quad \hat{\mathbf{B}} = \begin{bmatrix} \mathbf{K}^0 & \mathbf{0} \\ \mathbf{0} & -\mathbf{M}^0 \end{bmatrix}. \tag{20}$$

The natural frequencies of the robot structure are obtained from the generalized eigenvalues of $\hat{\mathbf{A}}$ and $\hat{\mathbf{B}}$ matrices [38]:

$$f_r = \frac{\sqrt{\lambda_r\lambda_r^*}}{2\pi}, \quad \text{and} \quad \zeta_r = -\frac{\mathrm{Re}(\lambda_r)}{2\pi f_r}, \tag{21}$$

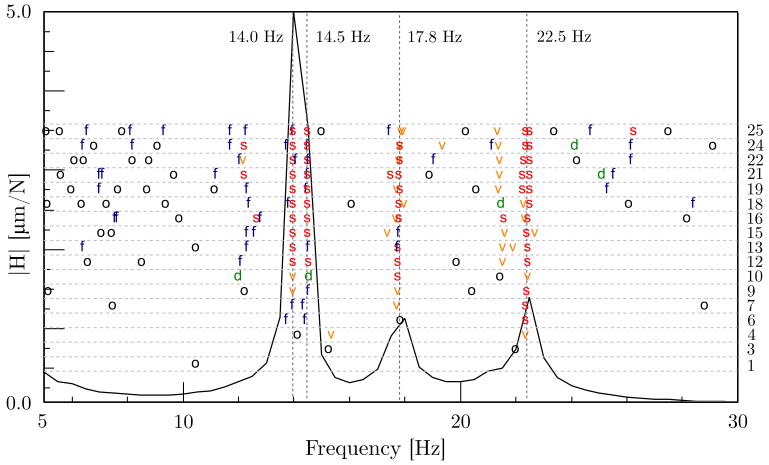

(a) Posture 1: rigid configuration

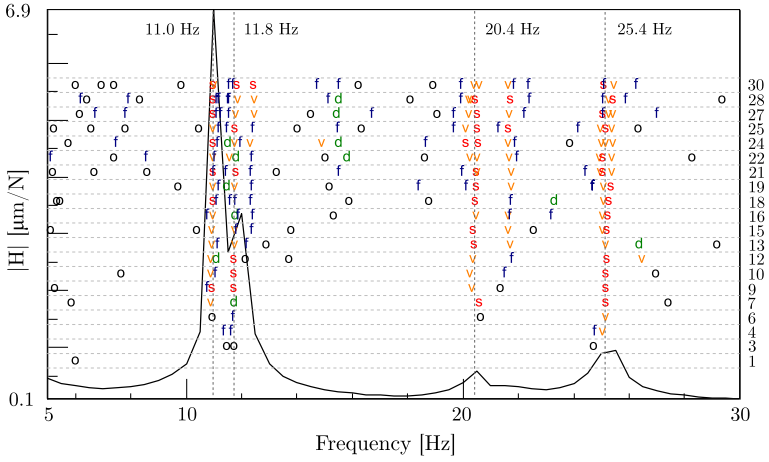

(b) Posture 2: upright configuration

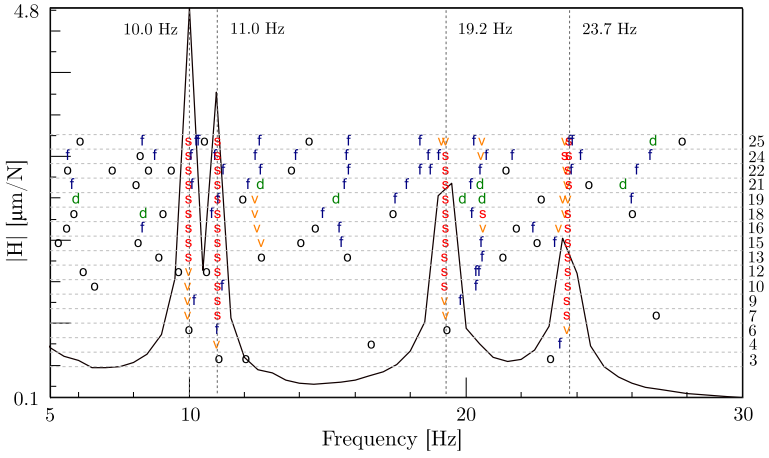

(c) Posture 3: milling configuration

Fig. 7. Stabilization diagrams of the LSCE modal identification in the three postures (right y-axis is the model order); meanings of the symbols: **o** pole not stable, **f** pole is stable in frequency, **d** pole is stable in frequency and damping, **v** pole vector is stable, **s** pole is completely stable.

where f_r and ζ_r, $r = 1..n$ ($n=3$) are the natural frequencies and the corresponding modal damping ratios, respectively. The asterisk stands for the complex conjugate, and λ_r are the generalized eigenvalues:

$$\hat{\mathbf{A}} v_r \lambda_r = \hat{\mathbf{B}} v_r. \tag{22}$$

Vectors v_r are the corresponding eigenvectors. Since $\hat{\mathbf{A}}$ and $\hat{\mathbf{B}}$ matrices are real, their generalized eigenvalues and eigenvectors appear in complex conjugate pairs. As a result, for the n-DOF arm, n pairs of eigenvectors and eigenvalues are obtained. Each pair of eigenvalues (λ_r, λ_r*) corresponds to one modal frequency (f_r), and each pair of

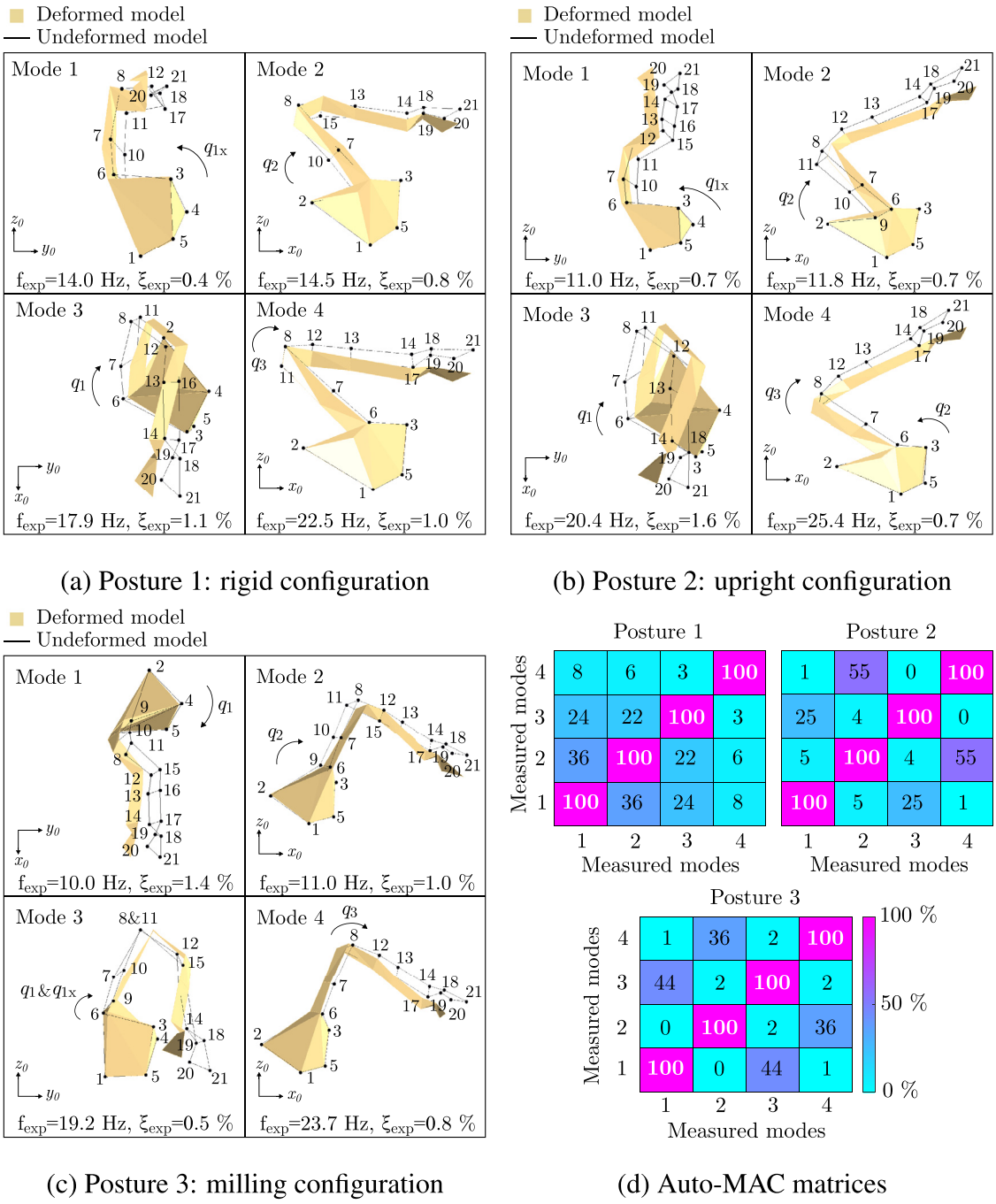

Fig. 8. Mode shapes identified using EMA in the three postures.

Table 3
Identified joint stiffness and damping parameters with the SDOF flexible joint model.

	Joint 1	Joint 2	Joint 3
Joint stiffness [Nm/rad]	3.12e6	3.75e6	2.98e6
Joint damping [Nm.s/rad]	1.45e3	1.10e3	0.29e3

eigenvectors (v_r, v_r^*) corresponds to the associated mode shape. Note that the resulting mode shape is in joint space, but obtaining the mode shape in Cartesian space is straightforward using forward kinematics.

The stiffness and damping parameters of the joints are determined by using the modal parameters obtained in Section 3. The modal parameters obtained from the milling posture are used for the identification of the joint parameters and the ones obtained from the other two postures will be used for the verification of the identified model.

Since the MBD model with SDOF joints includes three degrees of freedom ($n = 3$), only three modes can be created using this model, but four modes were identified from the modal analysis in Section 3. The identified mode three at 19.2 Hz in the milling posture includes a significant deflection of joint one around x_1 axis, which is not included in the SDOF joint model. Because the third mode in the milling posture cannot be simulated using the presented model, it will not be used in the identification. As discussed in Section 3, modes one, two, and four in the milling posture are associated with dominant deflections of joints one, two, and three around their rotation axis, respectively. The stiffness and damping coefficients of each joint can therefore be adjusted to

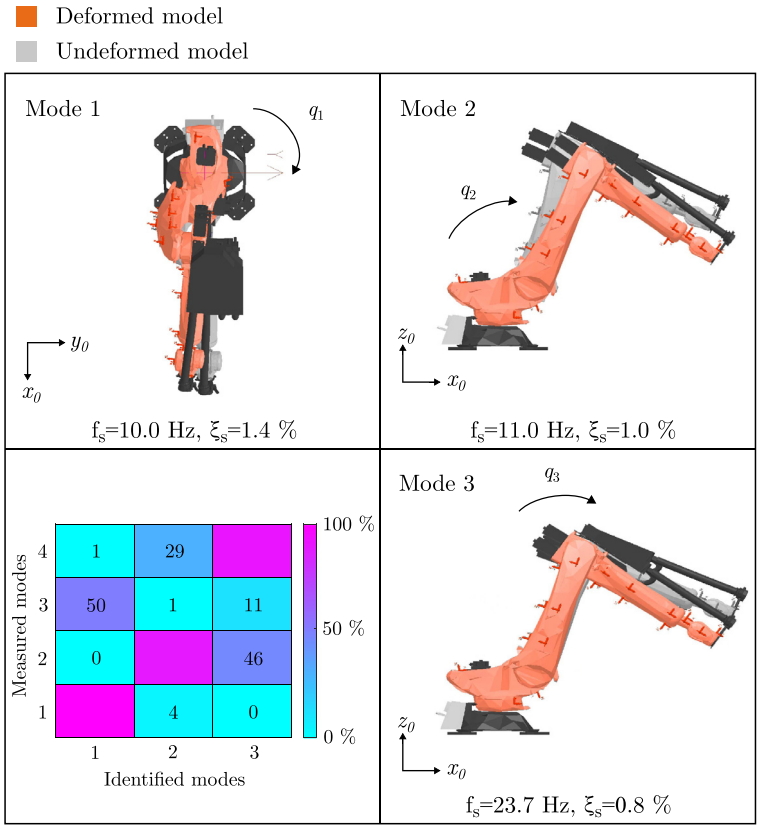

Fig. 9. Simulated mode shapes with the SDOF flexible joint model for the milling posture.

obtain the measured natural frequency and modal damping ratio for the associated mode. The resulting joint parameters are shown in Table 3.

The identified joint parameters are used in Eqs. (19)–(22) to obtain the frequency, damping ratio, and shape of the three modes of the MBD model with SDOF flexible joints in the three tested postures: milling, upright, and rigid.

The simulated mode shapes and associated modal frequencies and damping ratios in the milling posture are shown in Fig. 9. Compared to the measured mode shapes and modal parameters in the same posture, shown in Fig. 8c, the identified model predicts similar shapes, frequencies, and damping ratios. The third measured mode at 19.2 Hz is not predicted because the deflection of the first joint around x_1 axis is not included in the SDOF joint model. The MAC table in Fig. 9 shows the correlation between the measured and identified mode shapes in the milling posture. Neglecting the third measured mode, measured modes one, two, and four are highly correlated with simulated modes one, two, and three.

The identified modal parameters in the milling posture are used to construct the FRFs between the three DOFs at the robot flange, x_{21}, y_{21} and z_{21} (Fig. 6). The magnitudes of the resulting FRFs along with the corresponding measured FRFs are shown in Fig. 10. As depicted in this figure, except at around the mode at 19.2 Hz which is not predictable using the SDOF joint model, a reasonable agreement is observed between the predicted and measured FRFs. The largest discrepancies are observed at modes with small amplitudes and in cross-FRFs. The modes with small amplitudes in the FRFs are more rigid and thus more difficult to excite. This makes their measurement more sensitive to noise and measurement inaccuracies. The measured cross-FRFs, in addition to being a few times more rigid than the direct-FRFs, show a considerable level of asymmetry (e.g $H_{xy} \neq H_{yx}$) which contradicts the linear self-adjoint system used to model the dynamics [39]. Inaccuracy in the impact direction during the hammer test might also amplify the phenomenon. The non-symmetry of the FRF matrix in articulated industrial robots has been reported in other research as well [15] and is a subject for further studies. In order to study the accuracy of the developed MBD model in predicting the structural vibrations of the robot in arbitrary postures, the identified model is used to compute the mode shapes and modal parameters in the upright and rigid postures. The MAC tables between the predicted and measured mode shapes in the rigid and upright postures are shown in Fig. 11a and Fig. 11b, respectively. In the upright posture, a high level of correlation is observed between the three predicted modes and measured modes two to four. In the rigid posture, although the second and third predicted modes are highly correlated with the third and fourth measured modes, the first predicted mode is not correlated with any of the measured ones. As shown in the stabilization diagram of modal identification in this posture (Fig. 8d), the difference between the frequencies of the first two identified modes is less than the resolution of measured FRFs (0.5 Hz). As a result, the identified mode shapes of these two modes are highly affected by measurement and identification errors.

Also the comparison between the predicted and measured modal frequencies and damping ratios in those two postures are shown in Table 4. The modes that cannot be predicted by the SDOF joint model are marked with /. As joint stiffness and damping were identified for the milling posture (posture 3), frequencies and damping ratios in this posture match the experimental ones. The most significant error in the prediction of modal frequencies is − 28% error observed in the second measured mode in the upright posture (20.4 Hz). Average frequency and damping ratio prediction errors are 12.8% and 41.2%, respectively.

5. Multi-body dynamic model with 3DOF flexible joints

As presented in Section 4, the MBD model with SDOF flexible joints can be identified using a combination of rigid body identification methods and EMA, however this model cannot be used to simulate the mode shapes involving joint deflections around an axis other than the

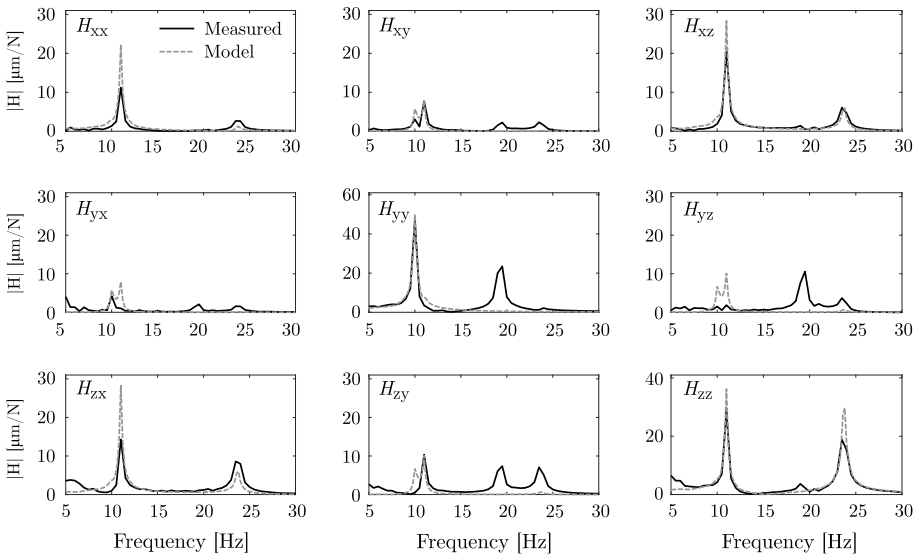

Fig. 10. Amplitude of measured and fitted frequency response function matrix $\mathbf{H}(\omega)$ at the end-effector obtained with the SDOF flexible joint model for the milling posture.

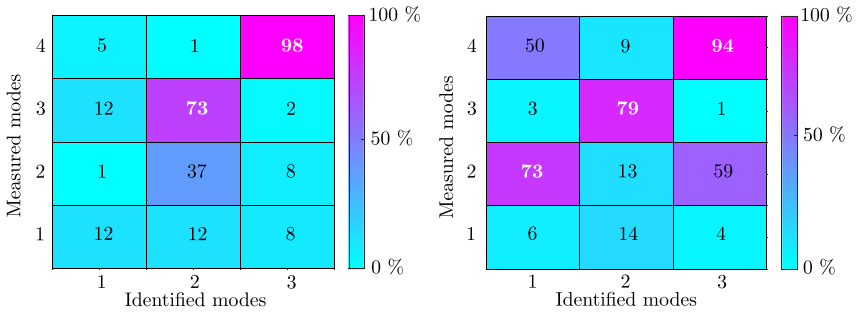

Fig. 11. Assessment of the posture dependency prediction through the MAC matrices.

Table 4
Prediction of the natural frequencies and damping ratios in other postures by using the identified SDOF flexible joint model (experimental frequencies and damping ratios in brackets).

Mode	Milling pose		Upright pose		Rigid pose	
	f_n [Hz]	ζ_n [%]	f_n [Hz]	ζ_n [%]	f_n [Hz]	ζ_n [%]
1	10.0 (10.0)	1.4 (1.4)	/ (11.0)	/ (0.7)	/ (14.0)	/ (0.5)
2	11.0 (11.0)	1.0 (1.0)	10.9 (11.8)	1.0 (0.7)	13.0 (14.5)	1.3 (0.8)
3	/ (19.2)	/ (0.5)	14.6 (20.4)	2.1 (1.6)	14.2 (17.8)	2.0 (1.2)
4	23.7 (23.7)	0.8 (0.8)	23.7 (25.4)	0.8 (0.7)	21.7 (22.5)	0.7 (1.0)

rotation axis. In order to capture the missing mode mainly involving a deflection of the first joint around x_1 axis, MBD model with 3DOF flexible joints shown in Fig. 1b is considered. Nevertheless, the inertia parameters of the model with 3DOF flexible joints cannot be identified using rigid body identification methods because only one out of the three DOFs per joint is actuated. Therefore, computer-aided design models of the robot are used as an entry point to estimate all the six parameters composing the inertia tensors of each link. The mass distribution is rebalanced with respect to the volume of each link and its associated density, bearing in mind the known total weight of the robot (1129 kg). Derivation of a similar robot model can be found in [40]. Using the mass matrix of the manipulator from the rigid body identification in the three studied postures for EMA, link inertia tensors are slightly adjusted for a better fitting. At present, the ad-hoc tuning of the

Table 5
Tuned Kuka KR90 dynamic parameters.

Mass [kg]	Shoulder 512	Arm 249	Forearm 223
I_{xx} [kg.m^2]	15.4	80.0	45.9
I_{yy} [kg.m^2]	30.9	150.6	125.9
I_{zz} [kg.m^2]	30.2	150.8	125.9
I_{xy} [kg.m^2]	1.9	−1.1	−1.4
I_{xz} [kg.m^2]	0.9	0.5	0.1
I_{yz} [kg.m^2]	0.4	−0.1	−1.2
C_x [m]	−0.02	0.53	0.42
C_y [m]	0	0	0.02
C_z [m]	−0.21	0.25	−0.02

mass matrix based on CAD data appears to be a common practice [28]. As part of this study, the rigid body identification allows relying on the determined base parameters as a guideline to tune the link inertia tensors. However, multiple sets of inertial parameters can be derived and lead to the same dynamic equations. Table 5 presents the tuned inertia parameters. The lumped parameters are eventually assigned to moving frames representing the robot links using the homogeneous transformation matrix formalism.

Joint elastic parameters are identified in the milling posture on the basis of the error between the simulated and measured frequencies and damping ratios in Section 3. The quadratic-like cost function was defined as

Table 6
Identified joint stiffness and damping for the 3DOF flexible joint model of the KUKA KR90 robot in the milling posture.

Joint stiffness [Nm/rad]			Joint damping [Nm.s/rad]		
k_1	k_{1x}	k_{1y}	d_1	d_{1x}	d_{1y}
5.0e6	6.1e6	11.9e6	0.02e3	0.04e3	3.1e3
k_2	k_{2x}	k_{2y}	d_2	d_{2x}	d_{2y}
6.9e6	11.8e6	8.1e6	2.4e3	0.04e3	9.4e3
k_3	k_{3x}	k_{3y}	d_3	d_{3x}	d_{3y}
2.8e6	5.2e6	12.0e6	0.2e3	9.2e3	0.08e3

$$J = \sum_{n=1}^{4} \left(W_f \left| \frac{f_{n,k} - f_{n,exp.}}{f_{n,exp.}} \right|^2 + W_\zeta \left| \frac{\zeta_{n,k} - \zeta_{n,exp.}}{\zeta_{n,exp.}} \right|^2 \right), \tag{23}$$

where subscript n is the mode number and k is the kth iteration [41]. Weighting coefficients on the frequency W_f and on the damping ratio W_ζ emphasize the quantities to fit in priority, the frequencies in this context ($W_f = 100$ and $W_\zeta = 1$). Normalization factors, $f_{n,exp.}$ and $\zeta_{n,exp.}$ are applied in order to include both the targeted experimental frequency $f_{n,exp.}$ and damping ratio $\zeta_{n,exp.}$ expressed in Hz and in %, respectively. The four experimental modes obtained in Section 3 in the milling posture were taken into account in the fitting procedure. Table 6 presents all the resulting elastic parameters which allow matching all the measured robot modes below 30 Hz. Regarding the stiffness values around the motion axes, values seem in accordance with the ones reported in the literature usually in the range of 0.1e6 to 7.0e6 Nm/rad [42]. On the other hand, stiffness values normal to the motion axes are unsurprisingly higher than the ones around the axes of motion. Determined joint damping values are more difficult to interpret but provide coherent damping ratios for the targeted modes. Overall, the determined elastic parameters are likely to be treated as fitting parameters without any physical meaning because of the uncertainty on the mass matrix identification.

In Fig. 12, the measured and fitted FRFs of the first four dominant structural modes of the robot are shown in the milling posture. Again only the amplitudes of the FRFs measured at the end effector are presented for points x_{21}, y_{21} and z_{21} (Fig. 6). The MBD model with 3DOF flexible joints is able to fit the missing peaks that the model with SDOF flexible joints could not replicate. Since the link inertia tensors were tuned with respect to the model identified through exciting trajectories, the quality of fitting regarding the direct-FRFs is preserved, while capturing the third mode at 19.2 Hz generating a deflection of the first joint around x_1 axis. Regarding the cross-FRFs, H_{xz}, presenting the highest amplitude, is particularly well correlated.

The updating of all the four mode shapes is confirmed by the high diagonal values shown in the MAC matrix (Fig. 13a). In comparison with the MAC matrix obtained with MBD model with the SDOF flexible joint representation in Section 4 (Fig. 9) for the milling posture, modes one, two and four show the same level of correlation. The third mode is now quite well correlated with 71%. Simulated mode shapes are presented in Fig. 13b. As before, mode shapes one, two and four, dominated by a deflection around the axes of motion, are captured and mode shape three highlights the sought combined deflections around and normal to the first joint (q_1 and q_{1x}).

The identified elastic parameters using the MBD model with the 3DOF flexible joint representation were eventually used to predict the modes in the rigid and upright postures. As a result, all the four mode shapes below 30 Hz could be reproduced and the resulting natural frequencies were closer to the experimental values than the ones reported in Table 4 using the SDOF flexible model (Table 7). Average frequency prediction error reduces to 5.5% from 12.8% when the SDOF joint model was used. However, the prediction on the damping ratios is worse since joint damping is affected by various factors such as the controller, the link flexibility and the gearbox. As shown in the MAC matrices in the predicted postures in Fig. 13a, correlated values for the rigid posture are still influenced by measurement and identification errors for the second mode as explained in Section 3. Otherwise, the first modes in the rigid and upright postures, which involved deflections normal to the first joint, are now captured. Mode shapes predicted in the upright posture follow the same trend as in the milling posture. High correlations are also observed between modes one and three and between modes two and four for the milling and upright postures as depicted in the measured auto-MAC matrices from Section 3 (Fig. 8d).

As a concluding remark, despite that simulated mode shapes in Fig. 13b showcase the most significant deflections, it is clear that smaller deviations arise around all the directions and for all the axes of the joints. For instance, the second mode of the milling posture is mainly dominated by a deflection around the second motion axis (q_2) but also requires the inclusion of DOF q_{1y} in order to faithfully reproduce the corresponding experimental mode shape. Therefore, all the elastic parameters of the MBD model with 3DOF flexible joints were taken into account even if only four modes were fitted.

6. Conclusion

A MBD model with SDOF joint model was presented to simulate the dynamics of an industrial robotic manipulator in machining

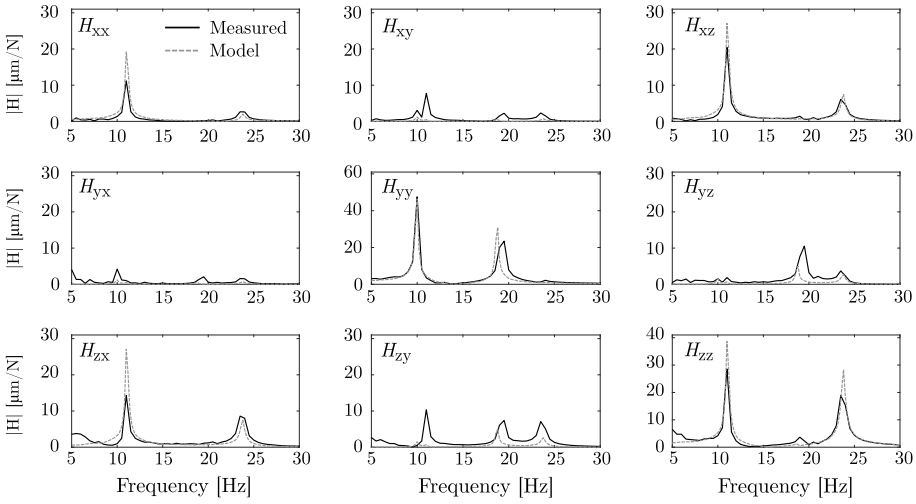

Fig. 12. Amplitude of measured and fitted frequency response function matrix $\mathbf{H}(\omega)$ at the end-effector obtained with the 3DOF flexible joint model for the milling posture.

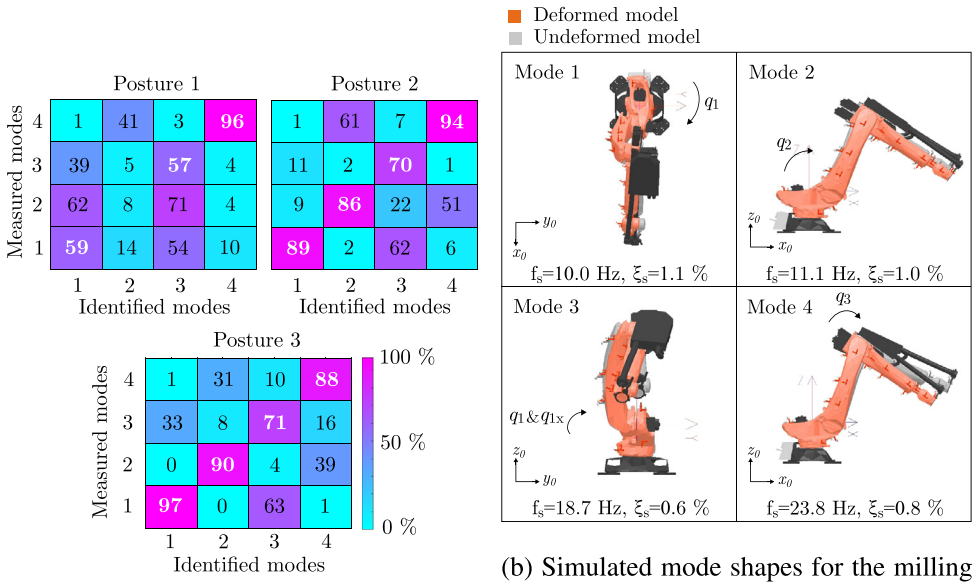

(a) Associated MAC matrices

(b) Simulated mode shapes for the milling posture

Fig. 13. Resulting vibrational modes obtained with the 3DOF flexible joint model.

Table 7
Prediction of the natural frequencies and damping ratios in other postures for the model involving 3DOF flexible joints (experimental frequencies and damping ratios in brackets).

Mode	Milling pose		Upright pose		Rigid pose	
	f_n [Hz]	ζ_n [%]	f_n [Hz]	ζ_n [%]	f_n [Hz]	ζ_n [%]
1	10.0 (10.0)	1.1 (1.4)	11.7 (11.0)	1.7 (0.7)	13.0 (14.0)	2.2 (0.5)
2	11.1 (11.0)	1.0 (1.0)	11.8 (11.8)	1.1 (0.7)	13.6 (14.5)	1.3 (0.8)
3	18.7 (19.2)	0.6 (0.5)	18.2 (20.4)	0.3 (1.6)	19.1 (17.8)	0.1 (1.2)
4	23.8 (23.7)	0.8 (0.8)	24.3 (25.4)	0.9 (0.7)	22.0 (22.5)	0.8 (1.0)

applications. The parameters of the model were identified using a combination of rigid body model identification method and experimental modal analysis.

The presented model can be used to predict the varying (posture-dependent) dynamics of the robot, which is essential for planning machining operations to avoid excessive vibrations and chatter. The presented identification approach is convenient to perform in industrial setups and does not require a detailed model of the link geometry.

A KUKA KR90 robotic arm was used as a case study, and it was shown that the presented MBD model with SDOF representation can fairly accurately simulate the vibration mode shapes in various postures. However, one mode shape that involved joint deflections around an axis perpendicular to the joint rotation axis could not be simulated using the presented model. The influence of the mode shapes that cannot be simulated on the overall dynamics may be different in various manipulators and also in various postures.

Consequently, a MBD model with 3DOF flexible joints was developed in order to capture all the measured mode shapes. However, such a model requires the knowledge of all the link inertia tensors. For that reason, a first guess of the inertial parameters was obtained using the CAD models of the links. The whole set of inertial parameters was then refined on the basis of the rigid body model identification results as a guideline in an ad-hoc method to tune the mass matrix of the manipulator. Thereafter, elastic parameters around and normal to the axes of motion were determined for one robot posture using a quadratic-like cost function. Note that the solution was not unique as the number of elastic parameters was higher than the number of measured modes thus leading to an underdetermined identification. Hence, the identified joint stiffness and damping ratios for the extended model did not have a physical meaning and were treated as fitting parameters. Finally, all posture-dependent modes were modelled, even those inducing deflections around axes perpendicular to the motion axes. The identified elastic parameters were eventually used to predict the robot natural frequencies, damping ratios and mode shapes in two other postures with a satisfying accuracy.

Declaration of Competing Interest

The authors declare that they do not have any financial or non-financial conflict of interests.

Acknowledgement

The authors would like to acknowledge the Belgian National Fund for Scientific Research (NFSR) for the grant allotted to H.N. Huynh, and the Natural Sciences and Engineering Research Council of Canada (grant no. RGPIN-2016-04284) for providing financial support under Discovery Grants program. The authors also thank the University of Victoria and Dynamic Optics for providing access to the KUKA KR90 R3100 HA robot.

Appendix A. Identified parameters

Appendix B. Regressor matrix

$$\mathbf{Y}(\mathbf{q}, \dot{\mathbf{q}}, \ddot{\mathbf{q}})\boldsymbol{\pi} = \boldsymbol{\tau} \tag{B.1}$$

Table A1
Base parameters of the Kuka KR90 R3100 robot and gravity compensation and friction coefficients.

i	Physical meaning of parameter i	Value
1	$I_{m,yy_2} + I_{m,yy_3} + I_{yy_2} + I_{yy_3} + I_{zz_1} + a_1^2(M_2 + M_3) + M_3 a_2^2 + M_{m_2} a_1^2 + M_{m_3} a_1^2 + M_{m_3} a_2^2 + I_{m,zz_1} N_1^2$	1897.8
2	$I_{zz_2} + M_3 a_2^2 + M_{m_3} a_2^2 + I_{m,zz_2} N_2^2$	1466.5
3	$M_3 a_2 + M_{m_3} a_2 + C_{x_2} M_2$	678.7
4	$C_{y_2} M_2$	48.3
5	$I_{xx_2} - I_{yy_2} - M_3 a_2^2 - M_{m_3} a_2^2$	−662.2
6	$I_{xz_2} + C_{z_3} M_3 a_2$	34.4
7	I_{xy_2}	91.9
8	I_{yz_2}	−1.0
9	I_{zz_3}	162.1
10	$C_{x_3} M_3$	129.1
11	$C_{y_3} M_3$	−2.7
12	$I_{xx_3} - I_{yy_3}$	−155.7
13	I_{xz_3}	1.4
14	I_{xy_3}	3.1
15	I_{yz_3}	−1.0
16	I_{m,zz_3}	0.0113
17	$I_{m,xx_2} - I_{m,yy_2}$	0.0147
18	$I_{m,xx_3} - I_{m,yy_3}$	0.0112
19	B_1	−7938.1
20	B_2	−72.8
21	B_3	257.1
22	F_{v_1}	5.4
23	F_{c_1}	1.2
24	F_{v_2}	5.0
25	F_{c_2}	1.4
26	F_{v_3}	3.7
27	F_{c_3}	0.9

$$\mathbf{Y} = \begin{bmatrix} Y_{1,1} & Y_{1,2} & \cdots & Y_{1,22} \\ Y_{2,1} & Y_{2,2} & \cdots & Y_{2,22} \\ Y_{3,1} & Y_{3,2} & \cdots & Y_{3,22} \end{bmatrix} \tag{B.2}$$

$$Y_{1,1} = \ddot{q}_1 \tag{B.3}$$

$$Y_{1,2} = Y_{1,9} = 0 \tag{B.4}$$

$$Y_{1,3} = 2a_1(\ddot{q}_1 \cos(q_2) - \dot{q}_1 \dot{q}_2 \sin(q_2)) \tag{B.5}$$

$$Y_{1,4} = -2a_1(\ddot{q}_1 \sin(q_2) + \dot{q}_1 \dot{q}_2 \cos(q_2)) \tag{B.6}$$

$$Y_{1,5} = \frac{\ddot{q}_1}{2} - \frac{\ddot{q}_1 \cos(2q_2)}{2} + \dot{q}_1 \dot{q}_2 \sin(2q_2) \tag{B.7}$$

$$Y_{1,6} = -\cos(q_2)\dot{q}_2^2 - \ddot{q}_2 \sin(q_2) \tag{B.8}$$

$$Y_{1,7} = -\ddot{q}_1 \sin(2q_2) - 2\dot{q}_1 \dot{q}_2 \cos(2q_2) \tag{B.9}$$

$$Y_{1,8} = \dot{q}_2^2 \sin(q_2) - \ddot{q}_2 \cos(q_2) \tag{B.10}$$

$$\begin{aligned} Y_{1,10} &= a_2 \ddot{q}_1 \cos(q_3) + a_2 \ddot{q}_1 \cos(2q_2 + q_3) + 2a_1 \ddot{q}_1 \cos(q_2 + q_3) \\ &\quad - 2a_1 \dot{q}_1 \dot{q}_2 \sin(q_2 + q_3) - 2a_1 \dot{q}_1 \dot{q}_3 \sin(q_2 + q_3) - a_2 \dot{q}_1 \dot{q}_3 \sin(q_3) \\ &\quad - 2a_2 \dot{q}_1 \dot{q}_2 \sin(2q_2 + q_3) - a_2 \dot{q}_1 \dot{q}_3 \sin(2q_2 + q_3) \end{aligned} \tag{B.11}$$

$$\begin{aligned} Y_{1,11} &= -a_2 \ddot{q}_1 \sin(q_3) - a_2 \ddot{q}_1 \sin(2q_2 + q_3) - 2a_1 \ddot{q}_1 \sin(q_2 + q_3) \\ &\quad - 2a_1 \dot{q}_1 \dot{q}_2 \cos(q_2 + q_3) - 2a_1 \dot{q}_1 \dot{q}_3 \cos(q_2 + q_3) - a_2 \dot{q}_1 \dot{q}_3 \cos(q_3) \\ &\quad - 2a_2 \dot{q}_1 \dot{q}_2 \cos(2q_2 + q_3) - a_2 \dot{q}_1 \dot{q}_3 \cos(2q_2 + q_3) \end{aligned} \tag{B.12}$$

$$\begin{aligned} Y_{1,12} &= \tfrac{\ddot{q}_1}{2} - \tfrac{\ddot{q}_1 \cos(2q_2 + 2q_3)}{2} + \dot{q}_1 \dot{q}_2 \sin(2q_2 + 2q_3) \\ &\quad + \dot{q}_1 \dot{q}_3 \sin(2q_2 + 2q_3) \end{aligned} \tag{B.13}$$

$$\begin{aligned} Y_{1,13} &= -\cos(q_2 + q_3)\dot{q}_2^2 - 2\cos(q_2 + q_3)\dot{q}_2 \dot{q}_3 \\ &\quad - \cos(q_2 + q_3)\dot{q}_3^2 - \ddot{q}_2 \sin(q_2 + q_3) - \ddot{q}_3 \sin(q_2 + q_3) \end{aligned} \tag{B.14}$$

$$Y_{1,14} = -\ddot{q}_1 \sin(2q_2 + 2q_3) - 2\dot{q}_1\dot{q}_2 \cos(2q_2 + 2q_3) - 2\dot{q}_1\dot{q}_3 \cos(2q_2 + 2q_3) \tag{B.15}$$

$$Y_{1,15} = \sin(q_2 + q_3)\dot{q}_2^2 + 2\sin(q_2 + q_3)\dot{q}_2\dot{q}_3 + \sin(q_2 + q_3)\dot{q}_3^2 - \ddot{q}_2 \cos(q_2 + q_3) - \ddot{q}_3 \cos(q_2 + q_3) \tag{B.16}$$

$$Y_{1,16} = 0 \tag{B.17}$$

$$Y_{1,17} = \frac{\ddot{q}_1}{2} - \frac{\ddot{q}_1 \cos(2N_2 q_2)}{2} + N_2\dot{q}_1\dot{q}_2 \sin(2N_2 q_2) \tag{B.18}$$

$$Y_{1,18} = \frac{\ddot{q}_1}{2} - \frac{\ddot{q}_1 \cos(2q_2 + 2N_3 q_3)}{2} + \dot{q}_1\dot{q}_2 \sin(2q_2 + 2N_3 q_3) + N_3\dot{q}_1\dot{q}_3 \sin(2q_2 + 2N_3 q_3) \tag{B.19}$$

$$Y_{2,1} = 0 \tag{B.20}$$

$$Y_{2,2} = \ddot{q}_2 \tag{B.21}$$

$$Y_{2,3} = a_1\dot{q}_1^2 \sin(q_2) - g\cos(q_2) \tag{B.22}$$

$$Y_{2,4} = a_1 \cos(q_2)\dot{q}_1^2 + g\sin(q_2) \tag{B.23}$$

$$Y_{2,5} = -\frac{\dot{q}_1^2 \sin(2q_2)}{2} \tag{B.24}$$

$$Y_{2,6} = -\ddot{q}_1 \sin(q_2) \tag{B.25}$$

$$Y_{2,7} = \dot{q}_1^2 \cos(2q_2) \tag{B.26}$$

$$Y_{2,8} = -\ddot{q}_1 \cos(q_2) \tag{B.27}$$

$$Y_{2,9} = \ddot{q}_2 + \ddot{q}_3 \tag{B.28}$$

$$Y_{2,10} = 2a_2\ddot{q}_2 \cos(q_3) - g\cos(q_2 + q_3) + a_2\ddot{q}_3 \cos(q_3) + a_1\dot{q}_1^2 \sin(q_2 + q_3) - a_2\dot{q}_3^2 \sin(q_3) + a_2\dot{q}_1^2 \sin(2q_2 + q_3) - 2a_2\dot{q}_2\dot{q}_3 \sin(q_3) \tag{B.29}$$

$$Y_{2,11} = g\sin(q_2 + q_3) - 2a_2\ddot{q}_2 \sin(q_3) - a_2\ddot{q}_3 \sin(q_3) + a_1\dot{q}_1^2 \cos(q_2 + q_3) - a_2\dot{q}_3^2 \cos(q_3) + a_2\dot{q}_1^2 \cos(2q_2 + q_3) - 2a_2\dot{q}_2\dot{q}_3 \cos(q_3) \tag{B.30}$$

$$Y_{2,12} = -\frac{\dot{q}_1^2 \sin(2q_2 + 2q_3)}{2} \tag{B.31}$$

$$Y_{2,13} = -\ddot{q}_1 \sin(q_2 + q_3) \tag{B.32}$$

$$Y_{2,14} = \dot{q}_1^2 \cos(2q_2 + 2q_3) \tag{B.33}$$

$$Y_{2,15} = -\ddot{q}_1 \cos(q_2 + q_3) \tag{B.34}$$

$$Y_{2,16} = \ddot{q}_2 + N_3\ddot{q}_3 \tag{B.35}$$

$$Y_{2,17} = -\frac{N_2\dot{q}_1^2 \sin(2N_2 q_2)}{2} \tag{B.36}$$

$$Y_{2,18} = -\frac{\dot{q}_1^2 \sin(2q_2 + 2N_3 q_3)}{2} \tag{B.37}$$

$$Y_{3,1} = Y_{3,2} = Y_{3,3} = Y_{3,4} = Y_{3,5} = Y_{3,6} = Y_{3,7} = Y_{3,8} = 0 \tag{B.38}$$

$$Y_{3,9} = \ddot{q}_2 + \ddot{q}_3 \tag{B.39}$$

$$Y_{3,10} = a_2\ddot{q}_2 \cos(q_3) - g\cos(q_2 + q_3) + a_1\dot{q}_1^2 \sin(q_2 + q_3) + \frac{a_2\dot{q}_1^2 \sin(q_3)}{2} + a_2\dot{q}_2^2 \sin(q_3) + \frac{a_2\dot{q}_1^2 \sin(2q_2 + q_3)}{2} \tag{B.40}$$

$$Y_{3,11} = g\sin(q_2 + q_3) - a_2\ddot{q}_2 \sin(q_3) + a_1\dot{q}_1^2 \cos(q_2 + q_3) + \frac{a_2\dot{q}_1^2 \cos(q_3)}{2} + a_2\dot{q}_2^2 \cos(q_3) + \frac{a_2\dot{q}_1^2 \cos(2q_2 + q_3)}{2} \tag{B.41}$$

$$Y_{3,12} = -\frac{\dot{q}_1^2 \sin(2q_2 + 2q_3)}{2} \tag{B.42}$$

$$Y_{3,13} = -\ddot{q}_1 \sin(q_2 + q_3) \tag{B.43}$$

$$Y_{3,14} = \dot{q}_1^2 \cos(2q_2 + 2q_3) \tag{B.44}$$

$$Y_{3,15} = -\ddot{q}_1 \cos(q_2 + q_3) \tag{B.45}$$

$$Y_{3,16} = N_3(\ddot{q}_2 + N_3\ddot{q}_3) \tag{B.46}$$

$$Y_{3,17} = 0 \tag{B.47}$$

$$Y_{3,18} = -\frac{N_3 \dot{q}_1^2 \sin(2q_2 + 2N_3 q_3)}{2} \tag{B.48}$$

References

[1] I. Iglesias, M.A. Sebastian, J.E. Ares, Overview of the state of robotic machining: Current situation and future potential, Procedia Eng. 132 (2015) 911–917.
[2] Y. Altintas, Manufacturing Automation: Metal Cutting Mechanics, Machine Tool Vibrations, and CNC Design, 2e edition, Cambridge University Press, 2012.
[3] Y. Altintas, E. Budak, Analytical prediction of stability lobes in milling, Ann. CIRP 44 (1995) 357–362.
[4] T. Insperger, B.P. Mann, G. Stépán, P.V. Bayly, Stability of up-milling and down-milling, part I: alternative analytical methods, Int. J. Mach. Tools Manuf. 43 (2003) 25–34.
[5] J. Tlusty, M. Polacek, The stability of the machine tool against self-excited vibration in machining, ASME Int. Res. Prod.Eng. (1963) 465–474.
[6] J. Tlusty, Manufacturing Processes and Equipment, Prentice Hall, Upper Saddle River, NJ, 2000.
[7] Z. Pan, H. Zhang, Analysis and suppression of chatter in robotic machining process, International Conference on Control, Automation and systems ICCAS, (2007), pp. 595–600.
[8] S.H.H. Zargarbashi, W. Khan, J. Angeles, Posture optimization in robot-assisted machining operations, Mech. Mach. Theory 51 (2012) 74–86.
[9] S. Mousavi, V. Gagnol, B.C. Bouzgarou, P. Ray, Dynamic behaviour model of a machining robot, ECCOMAS Multibody Dyn. (2013) 771–779.
[10] S. Mousavi, V. Gagnol, B.C. Bouzgarrou, P. Ray, Stability optimization in robotic milling through the control of functional redundancie, Robot. Comput. Integr. Manuf. (2017).
[11] S. Mousavi, V. Gagnol, B.C. Bouzgarrou, P. Ray, Dynamic model and stability prediction in robotic machining, Int. J. Adv. Manuf.Technol. (June 2016) 1–13.
[12] S. Mejri, V.G.T.-P. Le, L. Sabourin, P. Ray, P. Paultre, Dynamic characterization of machining robot and stability analysis, Int. J. Adv. Manuf. Technol. (2015).
[13] S. Mejri, Identification et Modélisation du Comportement Dynamique des Robots D'usinage (EN: Identification and Modelling of Milling Robot Dynamic Behaviour), Blaise Pascal University - Clermont-Ferrand II, 2016 PhD Thesis.
[14] D. Hajdu, T. Insperger, G. Stepan, The effect of non-symmetric FRF on machining: a case study, ASME 2015 International Design Engineering Technical Conferences and Computers and Information in Engineering Conference, Boston, Massachusetts, USA, August 2–5, (2015).
[15] M. Cordes, W. Hintze, Y. Altintas, Chatter stability in robotic milling, Robot. Comput. Integr. Manuf. 55 (2019) 11–18.
[16] S. Baglioni, F. Cianetti, C. Braccesi, D.M. De Micheli, Multibody modelling of n DOF robot arm assigned to milling manufacturing: dynamic analysis and position errors evaluation, J. Mech. Sci. Technol. 30(1) (2016) 405–420.
[17] G. Alici, B. Shirinzadeh, Enhanced stiffness modeling, identification and characterization for robot manipulators, IEEE Trans. Robot. 21 (4) (2005) 554–564.
[18] E. Abele, S. Rothenbücher, M. Weigold, Cartesian compliance model for industrial robots using virtual joints, Prod. Eng. 2 (3) (2008) 339–343.
[19] A. Pashkevich, A. Klimchik, D. Chablat, Enhanced stiffness modeling of manipulators with passive joints, Mech. Mach. Theory 46 (5) (2011) 662–679.
[20] A. Klimchik, A. Ambiehl, S. Garnier, B. Furet, A. Pashkevich, Efficiency evaluation of robots in machining applications using industrial performance measure, Robot. Comput. Integr. Manuf. (2017).
[21] M. Cordes, W. Hintze, Offline simulation of path deviation due to joint compliance and hysteresis for robot machining, Int. J. Adv. Manuf. Technol. 90 (2016) 1075–1083.
[22] T. Tjahjowidodo, F. Al-Bender, H.V. Brussel, On the chaotic response in a robot joint mechanism due to backlash, Proceedings of European Nonlinear Oscillations Conference ENOC, Eindohoven, Netherlands, (2005).
[23] A. Klimchik, D. Bondarenko, A. Pashkevich, S. Briot, B. Furet, Compliance error compensation in robotic-based milling, Informatics in Control, Automation and Robotics, Lectures Notes in Electrical Engineering, volumn 283, (2014), pp. 197–216 https://link.springer.com/chapter/10.1007%2F978-3-319-03500-0_13.
[24] A. Olabi, M. Damak, R. Bearée, O. Gibaru, S. Leleu, Improving the accuracy of industrial robots by offline compensation of joints errors, IEEE International Conference on Industrial Technology (ICIT 2012), (2012), pp. 492–497.
[25] C. Dumas, S. Caro, S. Garnier, B. Furet, Joint stiffness identification of six-revolute industrial serial robots, Robot. Comput. Integr. Manuf. 27 (2011) 881–888.
[26] J. Wang, H. Zhang, T. Fuhlbrigge, Improving machining accuracy with robot deformation compensation, IEEE/RSJ International Conference on Intelligent Robots and Systems, (2011).
[27] T. Hardeman, Modeling and Identification of Industrial Robots Including Drive and Joint Flexibilities, University of Twente, 2008 Ph.d. thesis.
[28] C. Reinl, M. Friedmann, J. Bauer, M. Pischan, E. Abele, O.V. Stryk, Model-based offline compensation of path deviation for industrial robots in milling applications, IEEE/ASME International Conference on Advanced Intelligent Mechatronics, (2011).
[29] J.J. Craig, Introduction to Robotic: Mechanics and Control, Pearson, Prentice Hall, 2005.
[30] B. Siciliano, O. Khatib, Handbook of Robotics, Springer-Verlag, 2007.
[31] J. Swevers, C. Ganseman, J. De Schutter, H.V. Brussel, Experimental robot identification using optimised periodic trajectories, Mech. Syst. Signal Process. 10 (5) (1996) 561–577.
[32] H. Mayeda, K. Yoshida, K. Osuka, Base parameters of manipulator dynamic models, IEEE Trans. Robot. Autom. 6 (3) (June 1990) 312–321.
[33] M. Gautier, W. Khalil, A direct determination of minimum inertial parameters of robots, Proceedings: IEEE International Conference on Robotics and Automation, (1998).
[34] L. Ljung, Signal Analysis and Prediction 163–173, Birkhauser, Boston, MA, 1998.
[35] J. Swevers, C. Ganseman, D.B. Tükel, J. De Schutter, H.V. Brussel, Optimal robot excitation and identification, IEEE Trans. Robot. Autom. 13 (5) (1997) 730–740.
[36] R. Brincker, C. Ventura, Introduction to Operational Modal Analysis, Wiley, 2015.
[37] Manufacturing Automation Laboratories, Cutpro, Manufacturing Automation Inc., Vancouver, BC, Canada, Accessed Nov. 20, 2017. Www.malinc.com
[38] N.M.M. Maia, J.M.M. Silva, Theoretical and Experimental Modal Analysis, John Wiley & Sons (1997).
[39] P. Elosegui, Measurement of the dynamic model of a PUMA 560 robot using experimental modal analysis, J. Mech. Des. (1994).
[40] H.N. Huynh, E. Rivière-Lorphèvre, O. Verlinden, Multibody modelling of a flexible 6-axis robot dedicated to robotic machining, IMSD: Proceedings of the 5th Joint International Conference on Multibody System Dynamics (Portugal, June, (2018).
[41] H.N. Huynh, G. Kouroussis, O. Verlinden, E. Rivière-Lorphèvre, Modal updating of a 6-axis robot for milling application, Proceeding of the 25th International Congress on Sound and Vibration, (July 2018).
[42] C. Dumas, S. Caro, C. Mehdi, S. Garnier, B. Furet, Joint Stiffness Identification of Industrial Serial Robots, Cambridge University Press, Robotica, 2011, pp. 1–20.